



Amorphous TiO₂ beats P25 in visible light photo-catalytic performance due to both total-internal-reflection boosted solar photothermal conversion and negative temperature coefficient of the forbidden bandwidth

Huiyu Yang^a, Jinyi Zhou^a, Zijian Duan^a, Xin Liu^a, Bo Deng^{a,*}, Jian Fang^{b,*}, Weilin Xu^a

^a State Key Laboratory of New Textile Materials and Advanced Processing Technologies, Wuhan Textile University, Wuhan 430200, China

^b College of Textile and Clothing Engineering, Soochow University, Suzhou 215000, China

ARTICLE INFO

Keywords:

Photothermal conversion
Total-internal-reflection
Atomic layer deposition
Amorphous titanium oxide
17 β -estradiol

ABSTRACT

In this work, visible light total reflective SiO₂@TiO₂ core-shell catalyst was synthesized by atomic layer deposition (ALD). This core-shell catalyst processing a total reflection character against full visible light favors the total effective traveling length of visible light inside the TiO₂ shell. Subsequently, higher catalyst temperature under visible light irradiation expands the light absorbing window of amorphous TiO₂ to full visible light due to its negative temperature coefficient of the forbidden bandwidth. Boosted photothermal conversion efficiency (145% that of amorphous TiO₂) can be achieved to exhibit a 17 β -estrogen degradation rate 1.5 times that of the commercial P25 (a mixed TiO₂ crystal of 20% rutile and 80% anatase) and 2.9 times catalytic velocity that of P25. The boosted catalytic performance of SiO₂@TiO₂ core-shell catalyst is attributed by expanded visible-light absorption, boosted photothermal conversion efficiency, and prolonged carrier lifetime.

1. Introduction

Amorphous TiO₂ has rarely been used as a photocatalyst due to its poor catalytic performance derived from its disordered lattice which is full of defects and thus leads to a poor separation efficiency of photo-generated electron-hole pairs [1–3].

Therefore, most research have focused on enhancing the catalytic performance of crystalline TiO₂. So far, many chemical modifications including doping [4,5], dye sensitization [6,7], noble metal compounding [8,9], and semiconductor compounding [10], have been used to increase the number of defects, extend the light absorption range, and increase the separation efficiency of photogenerated electron and hole.

It is widely known that an increase in reaction temperature significantly increases the catalytic reaction rate [11,12], while the huge external energy needed to heat large amounts of water makes it impractical. It has been noted that photocatalysis by TiO₂ generally adopts only a small fraction of the photo energy by sole generating active free radicals to degrade pollutants. Most of the photo energy are wasted by thermal dissipation due to its low photothermal conversion efficiency.

In addition, as a typical semiconductor with a negative temperature coefficient of the forbidden bandwidth [13,14], increased temperature

of a catalytic system will decrease the forbidden bandwidth of the catalyst, extend the photo-response window of the catalyst to the visible region, and increase the photocatalytic degradation efficiency.

If we can increase the photothermal conversion efficiency of amorphous TiO₂, subsequently increased temperature of the catalytic system may first expand the light absorption window of TiO₂ from UV region to full visible light due to its negative temperature coefficient of the forbidden bandwidth. In addition, subsequently raised catalytic system temperature also facilitates the photo catalytic efficiency of TiO₂.

As we know, the arrival of light from a light dense medium to a light sparse medium and an angle of incidence greater than or equal to the critical angle are two necessary conditions for total reflection [15–17]. If we can fabricate a SiO₂@TiO₂ (amorphous phase) catalyst with total reflection character, the utilization efficiency of visible light will be significantly improved and thus boost the photocatalytic performance of amorphous TiO₂.

Different from the amorphous TiO₂ in the SiO₂@TiO₂ core-shell catalyst in our work, Hu et al. [18] also used the sol-gel method and calcination to synthesize high surface area mesoporous crystalline SiO₂@TiO₂ photocatalyst. However, the results showed that the photo response range of the catalyst was still limited in the UV region, and the remove of Rhodamine B was mainly due to physical adsorption.

* Corresponding authors.

E-mail addresses: dengjianguo88@outlook.com (B. Deng), jian.fang@suda.edu.cn (J. Fang).

<https://doi.org/10.1016/j.apcatb.2022.121299>

Received 8 January 2022; Received in revised form 12 February 2022; Accepted 7 March 2022

Available online 9 March 2022

0926-3373/© 2022 Elsevier B.V. All rights reserved.

Amorphous TiO_2 with a higher refractive index ($n = 2.75$) densely coated onto SiO_2 ($n = 1.45$) via atomic layer deposition (ALD) to construct a $\text{SiO}_2 @\text{TiO}_2$ core-shell catalyst with a total reflection character for visible light. The total reflection will significantly increase the total traveling length of light within the TiO_2 shell layer (Figs. 1 and S1), thus enhance the photothermal conversion efficiency with significantly improve photocatalytic efficiency by both heating the catalytic system under sunlight without any extra external energy and expanding the light absorption region from UV to full visible light due to its negative temperature coefficient of the forbidden bandwidth.

Theoretically, increased TiO_2 shell thickness prolongs the migration time of photogenerated electrons and holes to the outmost surface. This also increases the lifetime of both photogenerated electrons and holes and facilitates the separation efficiency of them [19,20].

Endocrine-disrupting compounds (EDCs) are chemicals that interfere with the endocrine system [21–23] and have drawn increasing attention due to their widespread presence in surface water and wastewater. Among EDCs, 17 β -estradiol in wastewater at a trace level has been determined to have the highest endocrine-disrupting activity [24–26]. However, trace amounts of EDCs are difficult to be removed by traditional treatment such as advanced oxidation processes (AOP). Therefore, 17 β -estradiol can be used as a model contaminant to examine the catalytic performance of different catalysts.

In this work, we report an amorphous $\text{TiO}_2 @\text{SiO}_2$ core-shell catalyst fabricated via ALD. ALD is a chemical vapor deposition technology with surface self-limiting reaction. The deposited film has high compactness, conformity, and uniformity, and can generate a dense and uniform TiO_2 shell layer on SiO_2 surface [27–29]. The total reflection structure and its heterogeneous compositions were inspired by the greenhouse effect (Fig. S1) which favors total effective traveling length of light inside TiO_2 shell. More importantly, higher environment temperature attributed to both widened light adsorption window (negative temperature coefficient effect of forbidden band width for amorphous TiO_2) and elevated photothermal conversion efficiency. The core-shell structure can achieve a 1.5 times 17 β -estrogen degradation rate that of the commercial P25 (mixed crystal of 20% rutile and 80% anatase) and a 2.9 times catalytic speed that of P25. The results have revealed the feasibility of surface engineering in resulting highly efficient photocatalytic amorphous TiO_2 for various applications.

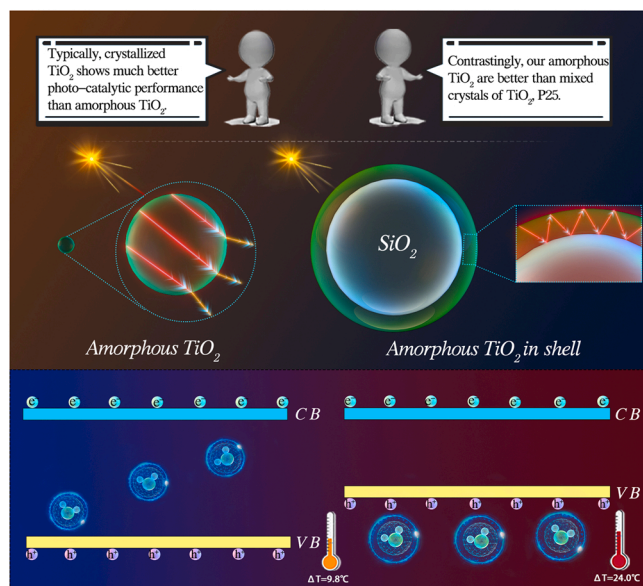


Fig. 1. Boosting mechanism of the photo-thermal effect on the catalytic performance of $\text{SiO}_2 @\text{TiO}_2$ -n catalyst.

2. Experimental section

2.1. Materials

Tetraethyl orthosilicate (TEOS, $\geq 99.0\%$), ammonium hydroxide ($\text{NH}_3 \cdot \text{H}_2\text{O}$, 25–28%), methanol (CH_3OH , $\geq 99.8\%$), sodium dodecyl benzene sulfonate (SDBS, $\geq 99.0\%$), and ethanol ($\text{C}_2\text{H}_5\text{OH}$, $\geq 99.7\%$) were purchased from Sinopharm Chemical Reagent Co., Ltd. 17 β -estradiol (E2, $> 97.0\%$) was supplied by Tokyo Chemical Industry Co., Ltd. Ethylene diamine tetra acetic acid (EDTA, $\geq 99.0\%$), p-benzoquinone (BQ, $\geq 99.0\%$), and Isopropanol ($\geq 99.0\%$) were provided by Shanghai Maclean Biochemical Technology Co., Ltd. Barium sulfate (BaSO_4 , $> 99.99\%$) was purchased from Aladdin reagent Co., Ltd.

Titanium (IV) isopropoxide (TIP, 99.999% metals basis, analytical grade) was obtained from Aladdin Industrial Co., Ltd. TiO_2 (P25, 20% rutile and 80% anatase) was purchased from Hefei Juwei Nano Technology Co., Ltd. The deionized water used in this experiment was obtained from a Milli-Q Plus 185 water purification system (Millipore, Bedford MA, USA) and had a resistivity of 10–16 $\text{M}\Omega \cdot \text{cm}$ at 25 °C. All the chemicals were used in this work without any further purification.

2.2. Preparation of SiO_2 micro-particles

The SiO_2 particles were prepared as reported [30]. Typically, $\text{NH}_3 \cdot \text{H}_2\text{O}$ (3.0 mL) was mixed with ethanol (16.25 mL) and deionized water (24.75 mL), and then stirred at a stirring speed of 1100 rpm under room temperature. This solution was recorded as solution A. TEOS (4.5 mL) was mixed with ethanol (45.5 mL) and magnetically stirred at 1100 rpm for 20 min, recorded as solution B.

Subsequently, solution B was quickly poured into solution A under magnetic stirring at a speed of 1000 rpm. After homogeneously mixing, the stirring speed was reduced to 400 rpm and kept for 20 h until the reaction completed. After the reaction, a centrifuge (TG16-WS, Hunan Michael Experimental Instrument Co., Ltd., China) was used at 10,000 rpm for 5 min to remove the supernatant of the obtained emulsion. The obtained white precipitate was washed with ethanol and centrifuged. After repeating the above process for three times, white SiO_2 particles were vacuum dried at 60 °C for 10 h.

2.3. Synthesis of $\text{SiO}_2 @\text{TiO}_2$ -n core-shell catalyst

TiO_2 was deposited onto SiO_2 particles by ALD in a self-made hot-wall closed chamber-type ALD reactor. Titanium (IV) isopropoxide (TIP) and deionized water (H_2O) were directly used as titanium and oxygen sources, respectively. High-purity nitrogen gas (N_2 , 99.999%, Wuhan Xiangyun Supply Co., Ltd.) was served as both carrying gas and purging gas at a steady flow of 50 standard cubic centimeters per minute (sccm) and a pressure of 60 Pa. TiO_2 was heated to 80 °C to provide sufficient vapor pressures while H_2O was maintained at room temperature. To prevent the condensation of TIP and deionized water, the delivery pipelines for the reactants were warmed up to 120 °C. The temperature of the ALD cavity was kept at 150 °C.

The ALD reaction cycle was performed as follow: TIP vapor and H_2O were alternatively pulsed into the reactor chamber with a duration of 0.2/8/20/0.05/8/20 s, corresponding to the TIP pulse/exposure/ N_2 purge/ H_2O pulse/ exposure/ N_2 purge, respectively. The schematic process of the fabrication of $\text{SiO}_2 @\text{TiO}_2$ core-shell structure is shown in Fig. S2. $\text{SiO}_2 @\text{TiO}_2$ -n indicates that n cycles of ALD TiO_2 were deposited onto SiO_2 .

2.4. Synthesis of control, amorphous TiO_2 , via sol-gel method

Amorphous TiO_2 with an averaged particle size of 55 nm was prepared by a one-step hydrolysis method. Specific steps are as follows: 5 mL tetrabutyl titanate was dropwisely added into 50 mL deionized water under a constant stirring (100 rpm). After stirring for 4 h, the

hydrolyzed tetrabutyl titanate was centrifuged and washed by deionized water for three times. Finally, the obtained white precipitate was dried at 80 °C. The XRD spectrum, SEM image, and size distribution curve of the amorphous TiO₂ are shown in Fig. S3.

2.5. Simulation calculation

The photothermal conversion process of core-shell SiO₂ @TiO₂ was established based on COMSOL Multiphysics 5.5 software. The scattering and absorption processes of light wave incident on the core-shell SiO₂ @TiO₂ were simulated using a wave optical module. The temperature change during light absorption was simulated by the solid heat transfer module. The schematic diagram of the calculation model is shown in Fig. S4. Due to the symmetry, only one-quarter of the core-shell SiO₂ @TiO₂ need to be established. The PMC (perfect magnetic conductor) symmetry plane and the PEC (scattering boundary condition) symmetry plane are involved in the simulation. The heat flux of incident light wave is 40 mW/cm², and the spectral range is consistent with that of sunlight. To compare the trend of temperature rise, the edges of particles were set as adiabatic to simulate the temperature rise process within 60 min under visible-light illumination.

2.6. Characterizations

Surface morphology and composition of SiO₂ @TiO₂ with different TiO₂ thickness were investigated by transmission electron microscope (TEM, JEOL JEM-2010, Japan Electronics Corporation, Japan) and Energy Dispersive X-ray analysis (EDX).

X-ray photoelectron spectroscopy (XPS, SPM-9700, SHIMADZU, Co. Ltd., Japan) was utilized to investigate the chemical composition of the SiO₂ @TiO₂-4000 and SiO₂ employing Al-K α (1486.6 eV) under ultra-high vacuum (UHV) (2×10^{-9} mbar).

UV–vis diffusion reflectance spectrum of the SiO₂ and SiO₂ @TiO₂-n were performed using a UV spectrophotometer (UV-2550, Shimadzu Co. Ltd, China) equipped with a diffuse reflectance accessory. Pure BaSO₄ was used as a reflectance standard in the UV–vis absorbance experiment.

The specific surface area and porous structures of the as-prepared samples were investigated under N₂ adsorption/desorption at −196 °C using a Micromeritics ASAP 2020 analyzer (Micromeritics ASAP 2020, Mike, USA). The specific surface area (S_{BET}) was calculated by the Brunauer-Emmett-Teller (BET) method. The total pore volume (V_{total}) was estimated by the liquid N₂ volume at a relative pressure of 0.98. The pore diameter and pore-size distribution were calculated by the Barrett-Joyner-Halenda (BJH) method.

X-ray diffraction (XRD) analysis was performed on an X'Pert PRO XRD spectrometer (X'Pert PRO, PANalytical, Holland) at a scanning rate of 10° min^{−1} in the 2 θ ranging from 5° to 80° at room temperature. The spectrometer was operated using a Cu-K α radiation source ($\lambda = 0.15405$ nm) at a generator voltage of 40 kV and a generator current of 50 mA, respectively.

The photocatalytic activities of the SiO₂ @TiO₂-n catalyst were conducted by photocatalytic degrading of 17 β -estradiol solutions (solvent: methanol) under simulated sunlight light using the xenon lamp (PL-X500D, Beijing Prince Technology Co., Ltd., China) with the fixed intensity of 40 mW/cm². The distance between the sample and light source was 15 cm. In a typical measurement, 0.5 g SiO₂ @TiO₂-n was first immersed and kept in 500 mL 17 β -estradiol solutions (5 mg/L) in the dark for 1 h without stirring to reach adsorption-desorption equilibrium. Then the reactor was exposed to the xenon lamp. Each 3 mL of the 17 β -estradiol solution was taken out at an interval of 15 min and examined by a UV spectrophotometer (UV-2550, Shimadzu Co. Ltd, China).

The photo-thermal conversion performance of SiO₂ @TiO₂-n was analyzed by using a 0.05 wt% SiO₂ @TiO₂-n aqueous suspension (0.01 wt% SDBS) on a self-made photo-thermal conversion device. Here, a xenon lamp with the fixed intensity of 40 mW/cm² was used to

simulate sunlight. The SiO₂ @TiO₂-n aqueous suspension was filled in a quartz cuvette with a size of 12.5 mm \times 12.5 mm \times 45 mm. The cuvette was wrapped by Silica Aerogel to isolate the energy exchange between the quartz cuvette and the external environment. The real-time temperature of the SiO₂ @TiO₂-n aqueous suspension was collected by a thermocouple connected with a digital thermometer (PM6501, Huayi Instrument, China).

Photoluminescence (PL) spectra of SiO₂ @TiO₂-4000 and P25 were characterized by a photoluminescence spectrometer (FLS980, Edinburgh Instruments Co. Ltd., UK). The time-resolved photoluminescence (TRPL) spectra were measured at room temperature on the same spectrometer (FLS980, Edinburgh Instruments Co. Ltd., UK) at an excitation source of 418 nm.

The transient photocurrent response was measured on an electrochemical analyzer (CHI660E, Chenhua Instruments Co. Ltd., China) using a Xe lamp ($\lambda > 420$ nm) as the light source. The working electrode was prepared by dip-coating the catalyst onto the surface of ITO glass. A platinum (Pt) wire was used as the counter electrode, and a Ag/AgCl (saturated KCl) was used as the reference electrode.

3. Results and discussion

3.1. Structure and morphology of SiO₂@TiO₂-n with different thickness of TiO₂ shell

The size and morphology of the SiO₂ and SiO₂ @TiO₂-n samples were investigated by a transmission electron microscopy (TEM). As shown in Fig. 2a, clear core-shell structure can be observed SiO₂ @TiO₂-4000. The calculated average diameter of the SiO₂ core was 520 \pm 19 nm (Fig. S5). Fig. 2b showed that the thickness of the TiO₂ shell of SiO₂ @TiO₂-4000 was about 30 nm. By plotting the relationship between TiO₂ shell thickness and ALD cycle number in Fig. 2c, it can be found that the thickness of the shell was linearly dependent on the ALD cycles, with a growth rate of 0.00785 nm/cycle. Compared with previously reported ALD process on silk fabrics [31], this growth rate was much slower, which may be due to both much fewer active sites on the SiO₂ core and its curved surface.

Corresponding element mapping of SiO₂ @TiO₂-4000 (Fig. 2d) further convinced that the TiO₂ shell was successfully coated onto the SiO₂ core in a dense manner. X-ray photoelectron spectroscopy (XPS) analysis (Fig. 2e) was performed on both SiO₂ and SiO₂ @TiO₂-4000. As expected, the characteristic Ti signal appeared in the spectrum of SiO₂ @TiO₂-4000. This indicated again that TiO₂ was successfully deposited onto the surface of the SiO₂ core. In addition, weakened Si signal of SiO₂ @TiO₂-4000 further implied the successful forming of the TiO₂ shell in SiO₂ @TiO₂-4000.

X-ray diffraction (XRD) spectra were collected to determine the phase composition of the SiO₂ core and the TiO₂ shell, as shown in Fig. 2f. A sole broad peak of SiO₂ located at near 23.7° indicated that the synthesized SiO₂ microparticles were amorphous [32,33]. Furthermore, the XRD patterns of the SiO₂ @TiO₂-n samples showed an amorphous phase of TiO₂ no matter the thickness of the TiO₂ shell. Besides, the reduced peak intensity of SiO₂ at around 23.7° along with increased thickness of TiO₂ shell could be explained by the covering effect of TiO₂.

The total effective light traveling length (L) had an almost linear dependence on the thickness of the TiO₂ shell (Fig. S1). Thus, the temperature of the SiO₂ @TiO₂-n samples will be increased due to augmented light-converted calorific value with increased TiO₂ shell thickness.

3.2. Theoretic simulation of photothermal conversion of TiO₂ and SiO₂@TiO₂

To understand the fundamental mechanism of the effect of surface engineering on the photothermal performance of TiO₂, a theoretic simulation was conducted using COMSOL Multiphysics 5.5 software.

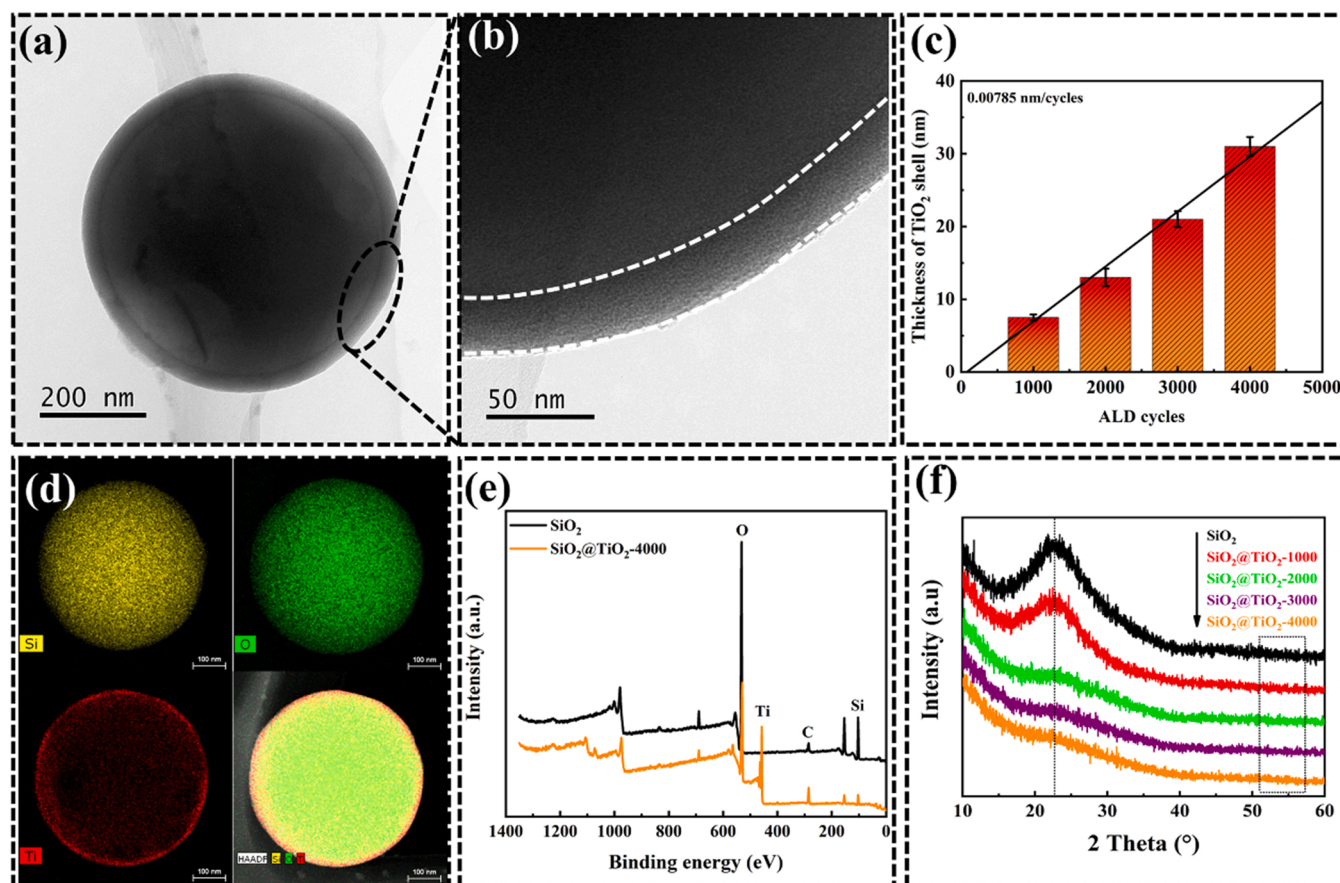


Fig. 2. (a–b) TEM images of SiO₂@TiO₂-4000 at different magnifications; (c) The relationship between TiO₂ shell thickness of SiO₂@TiO₂-n (averaged from three independent TEM images) and ALD cycle number; (d) Corresponding element mapping images of SiO₂@TiO₂-4000; (e) XPS spectra of the SiO₂ and the SiO₂@TiO₂-4000 samples; (f) XRD spectra of the SiO₂ and the SiO₂@TiO₂-n samples.

Based on a simulation model given in Fig. S4, risen temperature of SiO₂@TiO₂-4000 (4291 °C) is almost 40 folders that of TiO₂ (single ball) (586 °C) after being irradiated by 40 mW cm⁻² visible light for 60 min (Fig. 3a) in an adiabatic environment. Surprisingly, visible light absorbing power of SiO₂@TiO₂-n is around five orders of magnitude higher than that of TiO₂ (single ball) (Fig. 3b) with a TiO₂ domain size of 20 nm. Increased TiO₂ domain size resulted in a sharp decrease in the ratio of visible light absorbing power of SiO₂@TiO₂-n to that of TiO₂. Considering the decreased specific surface area with increased TiO₂ domain size, 10 nm is not optimal for a high performance TiO₂ photocatalyst. Much higher instantaneous body heat flow density distribution of SiO₂@TiO₂-4000 than that of TiO₂ (single ball) is clearly visible in Fig. 3c. Left figure in Fig. 3d shows that the intensity of the photoelectric field is mainly concentrated at the upper and lower boundaries of the single ball (TiO₂), indicating that most light passes through the particle without total reflection. By contrary, looking from top to bottom (light propagates from top to bottom) of SiO₂@TiO₂-4000 (right figure in Fig. 3d), the energy of the photoelectric field going out from the lower part is significantly reduced, indicating that a larger proportion of the light energy is total reflected and absorbed due to the obvious refractive index change directly in the inner and outer media.

3.3. Enhanced photothermal conversion and reduced bandgap of SiO₂@TiO₂-n

Amorphous TiO₂, P25, and SiO₂@TiO₂-n were detected by a UV-Vis diffuse reflectance spectrum (Fig. 4a). SiO₂ showed almost no absorption on the entire UV to visible light region (Fig. S6a) which was coincided with its photocatalytic inertness. Commercial TiO₂ catalyst, P25,

showed a weak absorption in the visible light region due to its limited photocatalytic activity inside the UV window [34–36].

The enhanced visible light absorption of SiO₂@TiO₂-n with increased ALD cycles subsequently enhanced its sunlight utilization efficiency. Generally, the darker color of catalyst will also enhance the visible light absorption. While in our case, the color of the catalyst, SiO₂@TiO₂-n, retains its original white color after ALD deposited by TiO₂. The bandgaps of amorphous TiO₂, P25 and SiO₂@TiO₂-n samples were calculated by the Kubelka-Munk method (Fig. 4b) and summarized in Table S1 [37–39].

SiO₂ micro-sphere had a bandgap of 3.71 eV which was higher than that of P25 (2.92 eV). This excluded the possibility of reduced bandgap of SiO₂@TiO₂-n was due to the reported coupling with narrower bandgap semiconductors [40]. A descending band gap sequence, SiO₂ > P25 > SiO₂@TiO₂-1000 > SiO₂@TiO₂-2000 > SiO₂@TiO₂-3000 > SiO₂@TiO₂-4000, is mainly caused by the increased thickness of the TiO₂ shell. The clear linear dependence of the bandgap of SiO₂@TiO₂-n with the thickness of the TiO₂ shell (Fig. 4c) further confirmed our bandgap tailoring mechanism (Fig. S1).

To calculate the photo-thermal conversion of different catalysts, the temperature of catalyst/water suspension was experimentally monitored after being exposed to sunlight for different periods of time (Figs. 4e and S7) on a home-made device (Fig. 4d). The results have revealed that the temperature of the SiO₂@TiO₂-n/water suspension was in positive correlation with the TiO₂ shell thickness (Fig. 4e).

TiO₂, as a negative temperature coefficient semiconductor, showed an increased temperature with reduced bad gap (Fig. 4f). Interestingly, different from the linear relationship between the bandgap and the TiO₂ shell thickness, an exponential inverse ratio of ΔT (increased

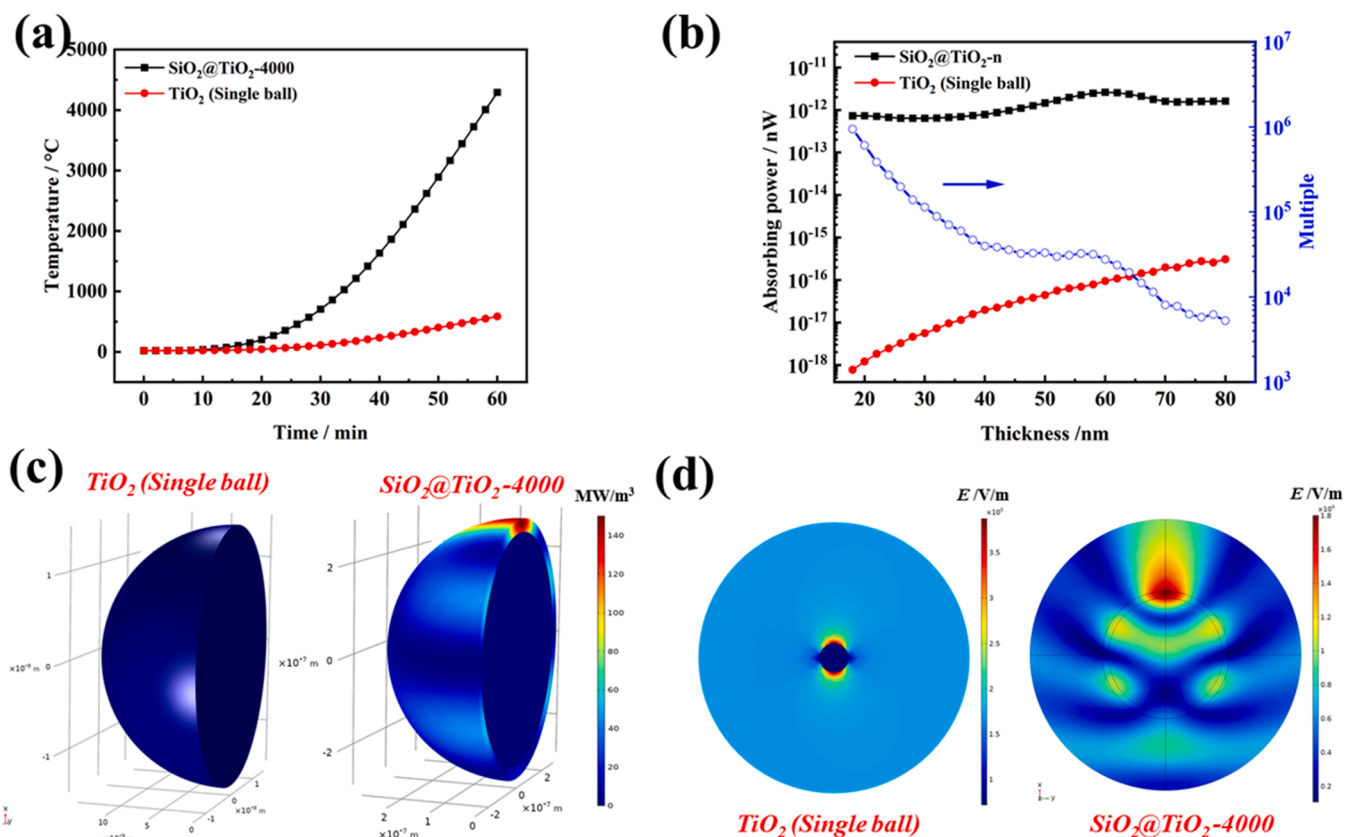


Fig. 3. (a) Risen temperature of SiO₂@TiO₂-4000 and TiO₂ (single ball) after irradiation by visible light at 40 mW cm⁻² in an adiabatic environment for different periods of time; (b) Visible light absorbing power of SiO₂@TiO₂-n and TiO₂ (single ball) as a function of shell thickness of SiO₂@TiO₂ (or diameter of TiO₂) under visible light at 40 mW cm⁻² in an adiabatic environment; (c) Instantaneous body heat flow density distribution of SiO₂@TiO₂-4000 and TiO₂ (single ball) under visible light at 40 mW cm⁻² with a TiO₂ domain size of 30 nm; (d) Instantaneous electric field distribution of SiO₂@TiO₂-4000 and TiO₂ (single ball) under visible light at 40 mW cm⁻² with a TiO₂ domain size of 30 nm.

temperature of SiO₂@TiO₂-n/water suspension compared with that of SiO₂/water suspension) to Δ Bandgap (reduced bandgap of SiO₂@TiO₂-n compared with that of SiO₂) was well coincided with previously reported results. [41,42].

The calorific value (denoted as Q) of each catalyst/water suspension was calculated according to Eq. (1) and plotted in Fig. 4g.

$$Q = C_p m (T_2 - T_1) \quad (1)$$

Where C_p is the specific heat capacity of water, m means the mass of catalyst/water suspension (mg), T_1 and T_2 represent the equilibrium temperature (K) of the suspension before and after light irradiation, respectively. Corresponding detailed data were summarized in Table S2.

The generated thermal energy of SiO₂@TiO₂-4000 (TiO₂ thickness of 30 nm) is around 2.45 times (2016.0 J/mg) that of single ball TiO₂ (823.0 J/mg) which affords for a significant aqueous suspension temperature rise of 15.4° after irradiated by visible light for 60 min (Fig. 4e).

The absorbed light energy (denoted as E_{PE}) was evaluated by the integrated area spanning from 200 to 800 nm (based on Fig. 4a). Thus, the photo-thermal conversion efficiency (CE_{PT}) could be expressed according to Eq. (2). Increased percentage in light-thermal conversion efficiency of various catalysts using amorphous TiO₂ as 100.0% was plotted in Fig. 4i.

$$CE_{PT} = \frac{Q}{E_{PE}} \quad (2)$$

Where Q and E_{PE} are the calorific value of catalyst/water suspension (Fig. 4g) and integrated area of absorbed light energy of catalyst

(Fig. 4h), respectively.

The SiO₂@TiO₂-4000 showed 145.0% and 127.0% light-thermal conversion efficiency that of amorphous TiO₂ and P25 (Fig. 4i), respectively. Both increased light adsorption and light-thermal conversion efficiency contribute to the increased catalyst/water suspension temperature after being irradiated by sunlight for the same period.

Specific surface area (S_{BET}) is an important factor affecting the photocatalytic performance of catalyst. To compare the pore structure of the SiO₂ and SiO₂@TiO₂-4000 samples, the specific surface area and pore size distribution were measured by the N₂ adsorption-desorption isotherm, as displayed in Fig. S8a. The S_{BET} of SiO₂@TiO₂-4000, as calculated by the BET method (Table S3), was only 4.95 m²/g, which was lower than that (6.83 m²/g) of an uncoated SiO₂. This was in accordance with the increased total diameter of SiO₂@TiO₂-4000 after coated by TiO₂. The decreased specific surface area of SiO₂@TiO₂-n indicated that the specific surface area does not contribute to the improved photocatalytic performance in our experiment.

3.4. Photocatalytic degradation mechanism and performance of SiO₂@TiO₂-n against 17 β -estradiol

17 β -estradiol was used as the model contaminant to examine the photo-catalytic performance of SiO₂@TiO₂ core-shell catalyst. Before the degradation experiment, the dark adsorption of SiO₂ and SiO₂@TiO₂-n was measured (Fig. S8b). The slightly higher dark adsorption of SiO₂ than that of SiO₂@TiO₂-n was consistent with higher specific surface area of the former.

Photocatalytic degradation curves of SiO₂, P25, and SiO₂@TiO₂-n against 17 β -estradiol under sunlight were compared in Fig. 5a.

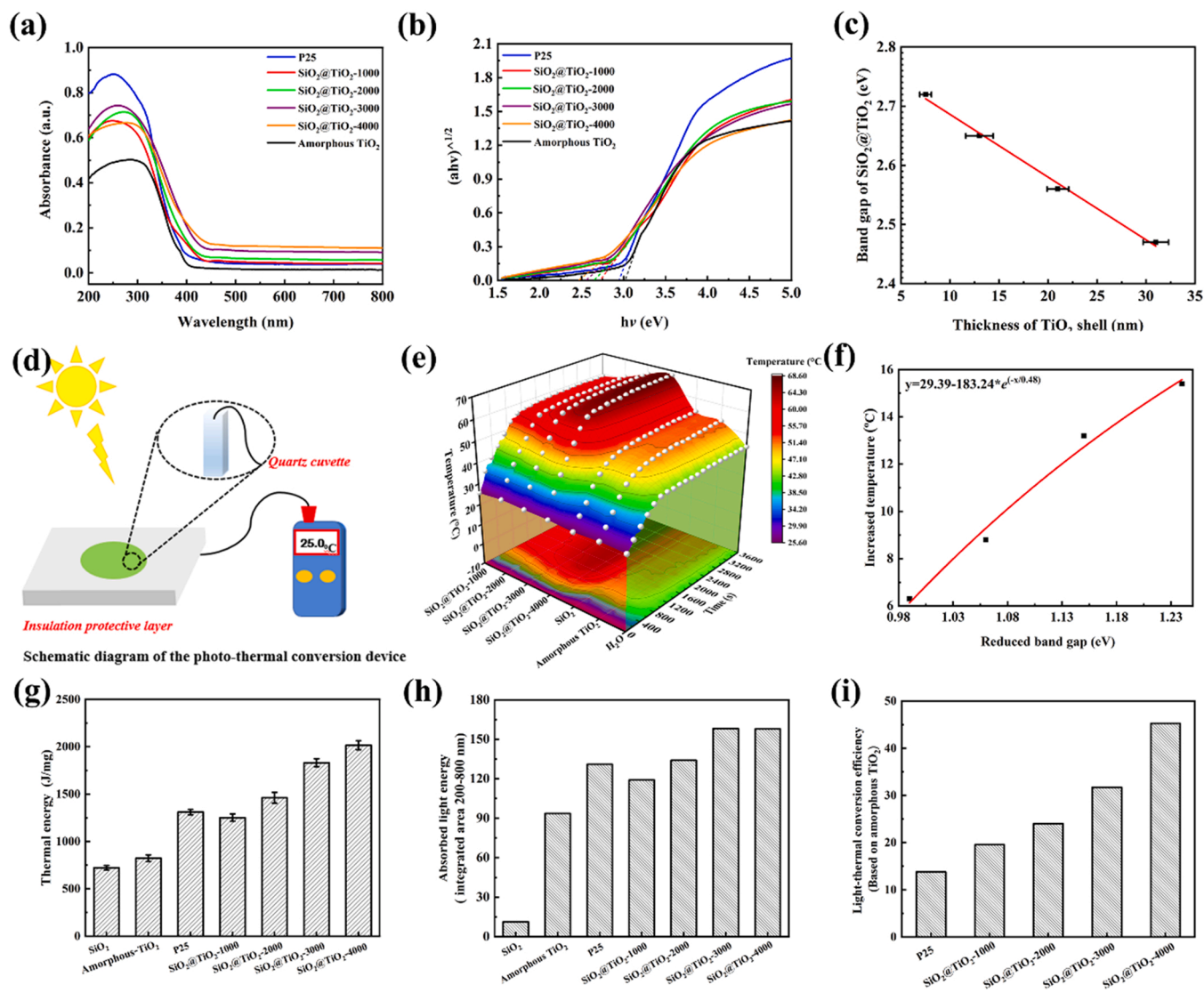


Fig. 4. (a) UV-Vis diffusion reflectance spectra of amorphous TiO₂, P25, and SiO₂@TiO₂-n; (b) Bandgap of the amorphous TiO₂, P25, and SiO₂@TiO₂-n calculated from the plots of $(\alpha h\nu)^{1/2}$ versus the photon energy ($h\nu$); (c) Effect of TiO₂ shell thickness on the corresponding band gap of different catalysts; (d) Schematic illustration of the home-made photo-thermal conversion test device; (e) Effect of visible light irradiation time on the temperature of various catalyst/water suspensions; (f) The fitting curve of the ΔT (increased equilibrium temperature of SiO₂@TiO₂-n/water suspension with the equilibrium temperature of SiO₂/water suspension as the base) as a function of Δ Band gap (reduced band gap of SiO₂@TiO₂-n compared with that of SiO₂); (g) Thermal energy generated by SiO₂, amorphous TiO₂, P25, and SiO₂@TiO₂-n after visible-light irradiation for 1 h; (h) Integrated area of absorbed light energy of SiO₂, amorphous TiO₂, P25, and SiO₂@TiO₂-n spanning from 200 to 800 nm; (i) Light-thermal conversion efficiency of P25 and SiO₂@TiO₂-n (based on amorphous TiO₂).

Typically, 0.5 g SiO₂, SiO₂@TiO₂-n, or P25 was immersed in 500 mL 17 β -estradiol aqueous solution (5 mg/L) for 80 min in dark to reach an adsorption-desorption equilibrium without stirring. Thereafter, the mixed solution was exposed to sunlight. As shown in Fig. 5c, SiO₂ revealed a 23.0% decrease in C_t/C_0 after the dynamic equilibrium of 150 min photo-catalysis. While the reduction ratio in C_t/C_0 of SiO₂@TiO₂-4000 was around 92.0%, which was significantly better than that of P25 (62.0%) under sunlight. The total 17 β -estradiol removal ratio of all catalysts adopted a sequence of SiO₂ < P25 < SiO₂@TiO₂-1000 < SiO₂@TiO₂-2000 < SiO₂@TiO₂-3000 < SiO₂@TiO₂-4000.

While the higher thickness of TiO₂ shell will significantly reduce the specific surface area of catalyst which result in a deteriorated catalytic performance of SiO₂@TiO₂-n. According to the theoretic simulation result (Fig. 3b), the optimal catalytic performance of SiO₂@TiO₂-n will be achieved at a TiO₂ shell thickness of around 58 nm.

Generally, the reduced band gap of SiO₂@TiO₂-4000 (Table S1) will lower the redox potential and thus weaken the photocatalytic ability of

catalyst. While the extended light active window to visible light (Fig. 4a) could utilize more sunlight to improve the photo-catalysis performance of catalysts.

The photocatalytic degradation kinetics of these samples were fitted to the pseudo-first-order (Fig. S9a) and second-order (Fig. S9b), respectively. The suitability of the two models was compared based on the corresponding correlation coefficient R^2 [43,44]. Fig. S9a showed the degradation rate constants of SiO₂, P25, and SiO₂@TiO₂-n for 17 β -estradiol under sunlight irradiation by plotting $-\ln(C_t/C_0)$ versus irradiation time. Calculated degradation rate constants of SiO₂, P25, and SiO₂@TiO₂-4000 from the fitted straight lines are 0.00274, 0.00616, and 0.01780 min⁻¹, respectively. This also demonstrated that the degradation rate of SiO₂@TiO₂-4000 was 2.9 times that of P25 under sunlight. Summarized photo-degradation kinetic parameters of SiO₂, P25, and SiO₂@TiO₂-n were given in Table S4. A higher correlation coefficient of R_2^2 than R_1^2 indicated that the degradation procedures of 17 β -estradiol by SiO₂, P25, and SiO₂@TiO₂-n were more accurately

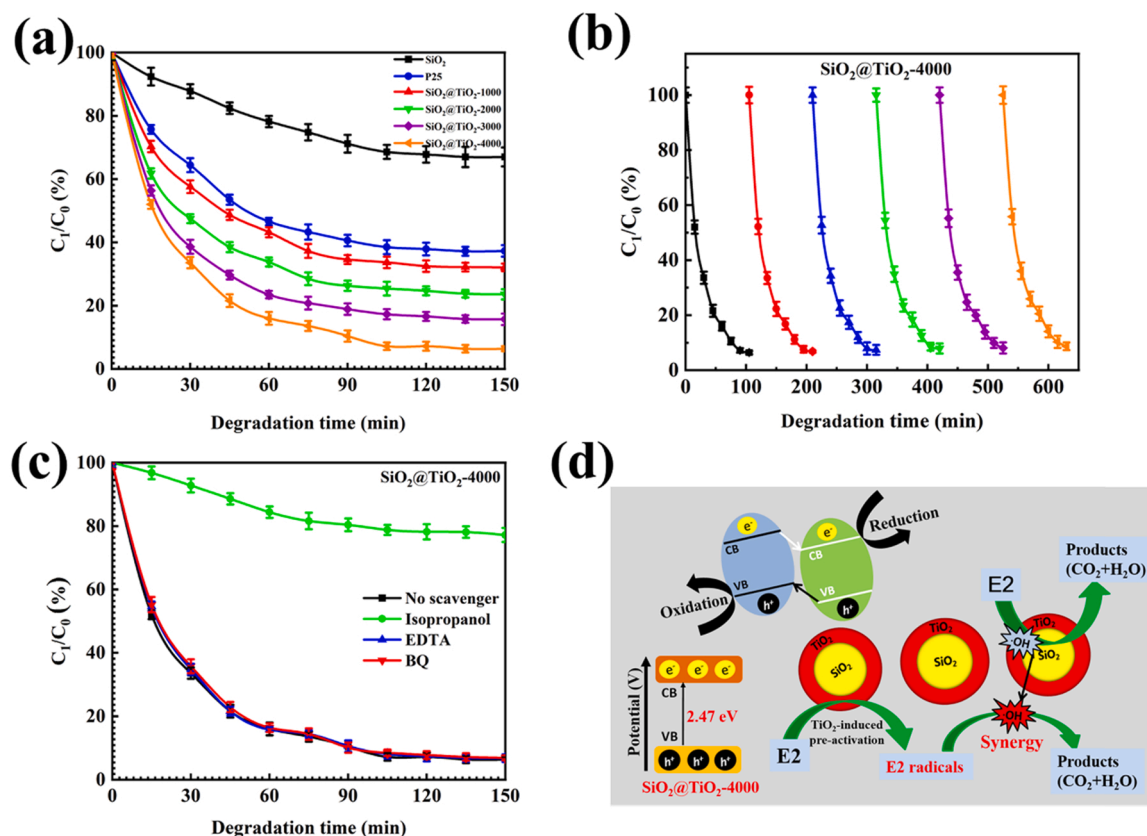


Fig. 5. (a) Time-dependent photo-catalytic 17β-estradiol degradation curves of SiO₂, P25, and SiO₂@TiO₂-n under sunlight; (b) Photocatalytic degradation curves of 17β-estradiol by SiO₂@TiO₂-4000 under visible light after repeated degradation cycles; (c) Photocatalytic degradation of 17β-estradiol by SiO₂@TiO₂-4000 in the presence of various free radical scavengers (initial 17β-estradiol=5 mg/L, scavenger concentration=1 mM); (d) Schematic illustration of proposed degradation mechanism of 17β-estradiol by SiO₂@TiO₂-n.

described by a pseudo-second-order model.

Recyclability and reusability which directly determine its service life are two important concerns for the practical application of a photocatalyst. To evaluate the recyclability and reusability of the photocatalyst, the SiO₂@TiO₂-4000 samples were repeated utilized to degrade 17β-estradiol under sunlight as shown in Fig. 5b. The catalyst was taken out after each cycle of catalysis experiment and rinsed with deionized water to remove residues. Then the aqueous suspension was centrifuged at 500 rpm for 3 min to obtain white SiO₂@TiO₂-4000 precipitate. This precipitate was oven-dried at 80 °C until constant weight obtained for the further catalytic experiment. The above catalytic experiment was repeated for 6 times. As can be seen (Fig. 5b), the photocatalytic ability of SiO₂@TiO₂-4000 was almost unchanged even after 6 cycles of degradation experiments, with a 17β-estradiol removal ratio up to 91.3%. These results revealed that SiO₂@TiO₂-4000 remained its good photocatalytic activity under sunlight after six photocatalytic cycles.

To evaluate the roles of h⁺, •OH, and •O₂⁻ in the degradation of 17β-estradiol, a widely used scavenger-quenching method was employed in the SiO₂@TiO₂-n catalytic system [45]. Isopropanol, EDTA, or BQ with a concentration of 1 mM was added into each parallel catalytic system separately. Fig. 5c showed that the addition of isopropanol significantly inhibited the photocatalytic reaction evidenced by a sharp decrease in removal efficiency, from 93.8% to 22.8%. The specific quenching species of isopropanol is •OH radical [46,47], suggesting that •OH radical played the most important role in the photo-degradation of 17β-estradiol under sunlight. Here, the removal of 17β-estradiol (22.8%) may be attributed to the direct oxidation of SiO₂@TiO₂-4000 [48]. In comparison, •O₂⁻ and h⁺ played a negligible role in the photocatalytic degradation of 17β-estradiol as the addition of BQ and EDTA did not

significantly change the corresponding photocatalytic degradation efficiencies [49,50]. These findings proved that •OH was the primary specie for 17β-estradiol degradations. The whole catalytic mechanism was proposed and illustrated in Fig. 5d. Equations to explain the detailed catalytic mechanism were given in the Supporting Material.

Besides the thermal-relevant boosting effect for catalytic performance, increased thickness of the TiO₂ shell prolongs the migration time of photogenerated electrons and holes (inside TiO₂ shell) to the outmost surface. This increases the lifetime of both photogenerated electrons and holes and improves the separation efficiency of them. To verify this mechanism, the photoluminescence spectroscopy (PL) of P25 and SiO₂@TiO₂-4000 was plotted in Fig. 6a (the excitation wavelength: 418 nm, as shown in Fig. S10). The calculated decay time of transient fluorescence (induced by the recombination of electron and hole) of P25 and SiO₂@TiO₂-4000 were 7.59 ns and 8.31 ns, respectively (Fig. 6b). The photocurrent density of P25 and SiO₂@TiO₂-4000 are 0.84 and 0.90 μA, respectively (Fig. 6c). Both of these results convince a longer lifetime of photogenerated electron and hole of SiO₂@TiO₂-4000 than that of P25.

4. Conclusions

In summary, previous research on improving photocatalytic performance of TiO₂ have been generally focused on their chemical structure modulation. Our work emphasizes that the physical structure of photocatalyst should not be ignored. Photo-thermal converted thermal energy could be hardly utilized in previous TiO₂-based catalysis due to their poor photo-thermal conversion. Ingenious core-shell structure can significantly increase the photothermal conversion efficiency of amorphous TiO₂ by 45.0% to heat the entire catalytic aqueous system, thereby significantly increasing the catalytic efficiency and velocity. The

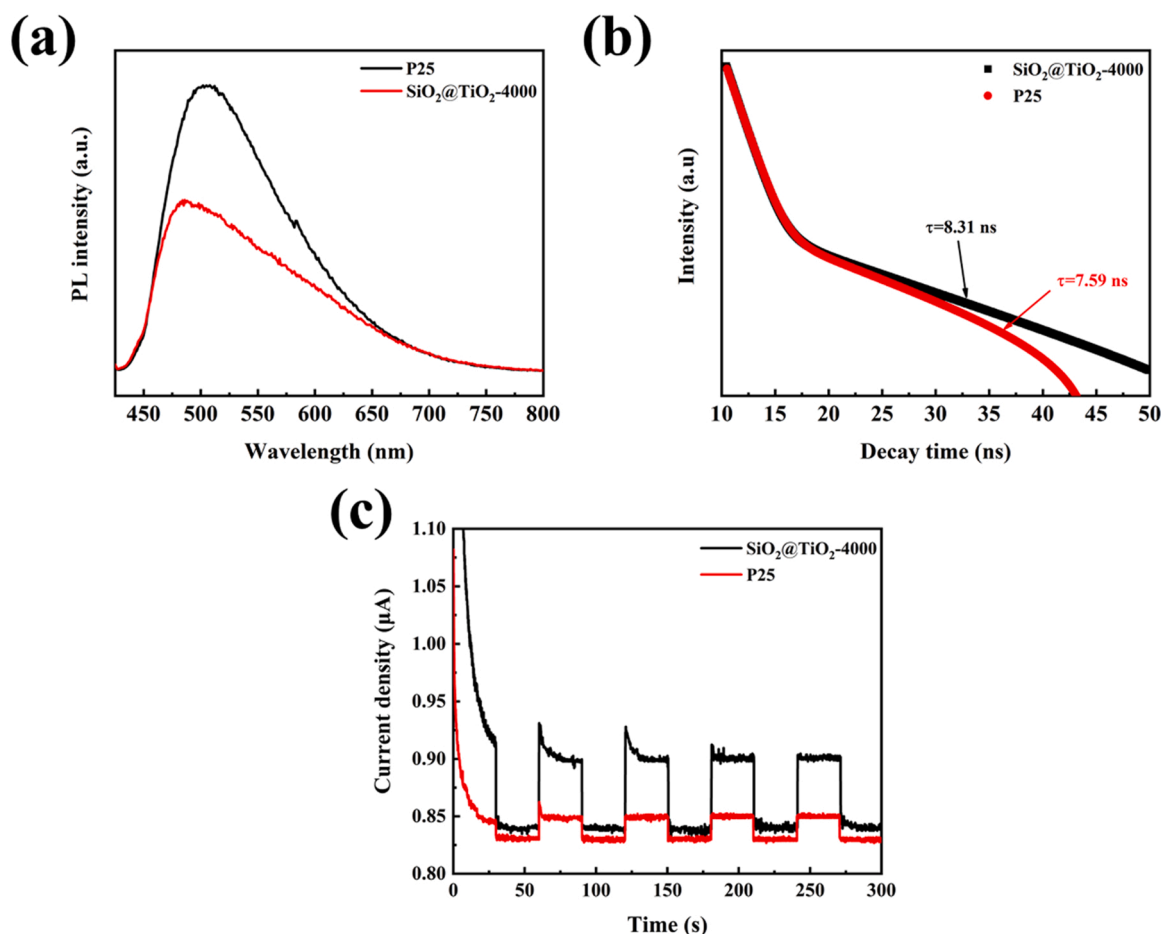


Fig. 6. (a) Photoluminescence spectra and (b) time-resolved photoluminescence of SiO₂@TiO₂-4000 and P25, respectively (with an excitation wavelength of 418 nm); (c) Photocurrent response of SiO₂@TiO₂-4000 and P25.

modified core-shell structured SiO₂@TiO₂-4000 exhibited 1.5 times the photocatalytic capacity and 2.9 times the catalytic speed of P25, respectively, without altering its amorphous phase.

CRediT authorship contribution statement

Huiyu Yang: Methodology, Formal analysis, Writing – original draft. **Jinyi Zhou:** Validation, Investigation. **Zijian Duan:** Validation, Investigation. **Xin Liu:** Validation, Investigation. **Bo Deng:** Conceptualization, Resources, Writing – review & editing, Supervision, Project. **Jian Fang:** Writing – review & editing, Supervision, Project. **Weilin Xu:** Supervision, Funding acquisition.

Declaration of Competing Interest

The authors declare that they have no known competing financial interests or personal relationships that could have appeared to influence the work reported in this paper.

Acknowledgments

This work was supported by the National Natural Science Foundation of China (Grant 51773158, 52173059) and the Key Laboratory of Textile Fiber&Product (Wuhan Textile University) (Grant FZXW2017013), Ministry of Education.

Appendix A. Supporting information

Supplementary data associated with this article can be found in the online version at [doi:10.1016/j.apcatb.2022.121299](https://doi.org/10.1016/j.apcatb.2022.121299).

References

- [1] H. Liang, Q. Meng, X. Wang, H. Zhang, J. Wang, Nanoplasmonically engineered interfaces on amorphous TiO₂ for highly efficient photocatalysis in hydrogen evolution, *ACS Appl. Mater. Interfaces* 10 (2018) 14145–14152.
- [2] M. Torralvo, J. Sanz, I. Sobrados, J. Soria, C. Garlisi, G. Palmisano, S. Çetinkaya, S. Yurdakal, V. Augugliaro, Anatase photocatalyst with supported low crystalline TiO₂: the influence of amorphous phase on the activity, *Appl. Catal. B* 221 (2018) 140–151.
- [3] J. Lyu, L. Zhou, J. Shao, Z. Zhou, J. Gao, Y. Dong, Z. Wang, J. Li, TiO₂ hollow heterophase junction with enhanced pollutant adsorption, light harvesting, and charge separation for photocatalytic degradation of volatile organic compounds, *Chem. Eng. J.* 391 (2020), 123602.
- [4] J. Pan, Z. Dong, B. Wang, Z. Jiang, C. Zhao, J. Wang, C. Song, Y. Zheng, C. Li, The enhancement of photocatalytic hydrogen production via Ti³⁺ self-doping black TiO₂/g-C₃N₄ hollow core-shell nano-heterojunction, *Appl. Catal. B* 242 (2019) 92–99.
- [5] Y. Wang, L. Rao, P. Wang, Z. Shi, L. Zhang, Photocatalytic activity of N-TiO₂/O-doped N vacancy g-C₃N₄ and the intermediates toxicity evaluation under tetracycline hydrochloride and Cr (VI) coexistence environment, *Appl. Catal. B* 262 (2020), 118308.
- [6] Y.-F. Chen, J.-F. Huang, M.-H. Shen, J.-M. Liu, L.-B. Huang, Y.-H. Zhong, S. Qin, J. Guo, C.-Y. Su, A porous hybrid material based on calixarene dye and TiO₂ demonstrating high and stable photocatalytic performance, *J. Mater. Chem. A* 7 (2019) 19852–19861.
- [7] X. Li, J.-L. Shi, H. Hao, X. Lang, Visible light-induced selective oxidation of alcohols with air by dye-sensitized TiO₂ photocatalysis, *Appl. Catal. B* 232 (2018) 260–267.
- [8] M. Macino, A.J. Barnes, S.M. Althabhan, R. Qu, E.K. Gibson, D.J. Morgan, S. J. Freakley, N. Dimitratos, C.J. Kiely, X. Gao, Tuning of catalytic sites in Pt/TiO₂

- catalysts for the chemoselective hydrogenation of 3-nitrostyrene, *Nat. Catal.* 2 (2019) 873–881.
- [9] A. Wang, Q. Zhu, Z. Xing, Multifunctional quaternized chitosan@surface plasmon resonance Ag/N-TiO₂ core-shell microsphere for synergistic adsorption-photothermal catalysis degradation of low-temperature wastewater and bacteriostasis under visible light, *Chem. Eng. J.* 393 (2020), 124781.
 - [10] C. Sun, Q. Xu, Y. Xie, Y. Ling, Y. Hou, Designed synthesis of anatase-TiO₂ (B) biphasic nanowire/ZnO nanoparticle heterojunction for enhanced photocatalysis, *J. Mater. Chem. A* 6 (2018) 8289–8298.
 - [11] S.X. Liang, Z. Jia, Y.J. Liu, W. Zhang, W. Wang, J. Lu, L.C. Zhang, Compelling rejuvenated catalytic performance in metallic glasses, *Adv. Mater.* 30 (2018), 1802764.
 - [12] A. Petala, P. Panagiotopoulou, Methanation of CO₂ over alkali-promoted Ru/TiO₂ catalysts: I. Effect of alkali additives on catalytic activity and selectivity, *Appl. Catal. B* 224 (2018) 919–927.
 - [13] Y. Cho, A. Yamaguchi, R. Uehara, S. Yasuhara, T. Hoshina, M. Miyauchi, Temperature dependence on bandgap of semiconductor photocatalysts, *J. Chem. Phys.* 152 (2020), 231101.
 - [14] P. Geng, W. Li, X. Zhang, X. Zhang, Y. Deng, H. Kou, A novel theoretical model for the temperature dependence of band gap energy in semiconductors, *J. Phys. D Appl. Phys.* 50 (2017), 40LT02.
 - [15] Y. Jin, J. Chang, Y. Shi, L. Shi, S. Hong, P. Wang, A highly flexible and washable nonwoven photothermal cloth for efficient and practical solar steam generation, *J. Mater. Chem. A* 6 (2018) 7942–7949.
 - [16] A. Farmani, A. Mir, Z. Sharifpour, Broadly tunable and bidirectional terahertz graphene plasmonic switch based on enhanced Goos-Hänchen effect, *Appl. Surf. Sci.* 453 (2018) 358–364.
 - [17] M.M. Ito, A.H. Gibbons, D. Qin, D. Yamamoto, H. Jiang, D. Yamaguchi, K. Tanaka, E. Sivanian, Structural colour using organized microfibrillation in glassy polymer films, *Nature* 570 (2019) 363–367.
 - [18] J.L. Hu, H.S. Qian, J.J. Li, Y. Hu, Z.Q. Li, S.H. Yu, Synthesis of mesoporous SiO₂@TiO₂ core/shell nanospheres with enhanced photocatalytic properties, *Part. Part. Syst. Charact.* 30 (2013) 306–310.
 - [19] F. Zhang, X. Li, Q. Zhao, G. Chen, Q. Zhang, High-performance In₂O₃@PANI core@shell architectures with ultralong charge carriers lifetime for photocatalytic degradation of gaseous 1, 2-dichlorobenzene, *Appl. Catal. B* 263 (2020), 118278.
 - [20] H. Li, T. Hu, J. Liu, S. Song, N. Du, R. Zhang, W. Hou, Thickness-dependent photocatalytic activity of bismuth oxybromide nanosheets with highly exposed (0 1 0) facets, *Appl. Catal. B* 182 (2016) 431–438.
 - [21] Z.-h. Liu, Z. Dang, H. Yin, Y. Liu, Making waves: Improving removal performance of conventional wastewater treatment plants on endocrine disrupting compounds (EDCs): their conjugates matter, *Water Res.* 188 (2021), 116469.
 - [22] E.B. Simsek, Solvothermal synthesized boron doped TiO₂ catalysts: photocatalytic degradation of endocrine disrupting compounds and pharmaceuticals under visible light irradiation, *Appl. Catal. B* 200 (2017) 309–322.
 - [23] C.M. Park, J. Heo, D. Wang, C. Su, Y. Yoon, Heterogeneous activation of persulfate by reduced graphene oxide–elemental silver/magnetite nanohybrids for the oxidative degradation of pharmaceuticals and endocrine disrupting compounds in water, *Appl. Catal. B* 225 (2018) 91–99.
 - [24] J. Cai, Y. Zhu, S. Xie, B. Niu, Y.-n. Zhang, L. Li, D. Li, G. Zhao, Accurate removal of trace 17 β -Estradiol and estrogenic activity in blended systems under a photoelectrocatalytic circulating flow, *Environ. Sci. Technol.* 55 (2021) 12585–12595.
 - [25] H.M. Nasir, S.Y. Wee, A.Z. Aris, L.C. Abdullah, I. Ismail, Processing of natural fibre and method improvement for removal of endocrine-disrupting compounds, *Chemosphere* (2021), 132726.
 - [26] X. Bai, K. Acharya, Removal of seven endocrine disrupting chemicals (EDCs) from municipal wastewater effluents by a freshwater green alga, *Environ. Pollut.* 247 (2019) 534–540.
 - [27] I. Spajić, P. Rodić, G. Šekularac, M. Lekka, L. Fedrizzi, I. Milošev, The effect of surface preparation on the protective properties of Al₂O₃ and HfO₂ thin films deposited on cp-titanium by atomic layer deposition, *Electrochim. Acta* 366 (2021), 137431.
 - [28] V.H. Nguyen, A. Sekkat, C. Jimenez, D. Munoz, D. Bellet, D. Munoz-Rojas, Impact of precursor exposure on process efficiency and film properties in spatial atomic layer deposition, *Chem. Eng. J.* 403 (2021), 126234.
 - [29] B. Wei, H. Chen, W. Hua, M. Chen, X. Ding, C. Li, Formation mechanism and photoelectric properties of Al₂O₃ film based on atomic layer deposition, *Appl. Surf. Sci.* 572 (2022), 151419.
 - [30] Y. Huiyu, K. Li, W. Liu, X. Liu, W. Xu, B. Deng, Development of structural colored cotton fabric via the layer-by-layer electrostatic self-assembling of SiO₂ nanoparticles, *Cellulose* 27 (2020) 4133–4144.
 - [31] H. Yang, Z. Yu, K. Li, L. Jiang, X. Liu, B. Deng, F. Chen, W. Xu, Facile and effective fabrication of highly UV-resistant silk fabrics with excellent laundering durability and thermal and chemical stabilities, *ACS Appl. Mater. Interfaces* 11 (2019) 27426–27434.
 - [32] Y. Zhang, R. Zhang, S. Chen, H. Gao, M. Li, X. Song, H.L. Xin, Z. Chen, Diatomite-derived hierarchical porous crystalline-amorphous network for high-performance and sustainable Si anodes, *Adv. Funct. Mater.* 30 (2020), 2005956.
 - [33] S.R. Almeida, C. Elicker, B.M. Vieira, T.H. Cabral, A.F. Silva, P.J. Sanches Filho, C. W. Raubach, C.A. Hartwig, M.F. Mesko, M.L. Moreira, Black SiO₂ nanoparticles obtained by pyrolysis of rice husk, *Dyes Pigments* 164 (2019) 272–278.
 - [34] S. Zhao, J. Chen, Y. Liu, Y. Jiang, C. Jiang, Z. Yin, Y. Xiao, S. Cao, Silver nanoparticles confined in shell-in-shell hollow TiO₂ manifesting efficiently photocatalytic activity and stability, *Chem. Eng. J.* 367 (2019) 249–259.
 - [35] L. Xu, L. Meng, X. Zhang, X. Mei, X. Guo, W. Li, P. Wang, L. Gan, Promoting Fe³⁺/Fe²⁺ cycling under visible light by synergistic interactions between P25 and small amount of Fenton reagents, *J. Hazard. Mater.* 379 (2019), 120795.
 - [36] W. Zhu, J. Mi, Y. Fu, D. Cui, C. Li, Multiple-cores@ shell clustered carbon dots/P25/rGO nanocomposite as robust visible-light photocatalyst for organic pollutant degradation and water disinfection, *Appl. Surf. Sci.* 538 (2021), 148087.
 - [37] P.K. Sharma, M.A.L. Cortes, J.W. Hamilton, Y. Han, J.A. Byrne, M. Nolan, Surface modification of TiO₂ with copper clusters for band gap narrowing, *Catal. Today* 321 (2019) 9–17.
 - [38] J.F. Guayaquil-Sosa, B. Serrano-Rosales, P.J. Valadés-Pelayo, H. de Lasa, Photocatalytic hydrogen production using mesoporous TiO₂ doped with Pt, *Appl. Catal. B* 211 (2017) 337–348.
 - [39] S. Kamimura, S. Yamashita, S. Abe, T. Tsubota, T. Ohno, Effect of core@shell (Au@Ag) nanostructure on surface plasmon-induced photocatalytic activity under visible light irradiation, *Appl. Surf. Sci.* 538 (2021), 148087.
 - [40] X. Zhao, C. Yao, T. Liu, J.C. Hamill Jr, G.O. Ngongang Ndjawa, G. Cheng, N. Yao, H. Meng, Y.L. Loo, Extending the photovoltaic response of perovskite solar cells into the near-infrared with a narrow-bandgap organic semiconductor, *Adv. Mater.* 31 (2019), 1904494.
 - [41] K. O'donnell, X. Chen, Temperature dependence of semiconductor band gaps, *Appl. Phys. Lett.* 58 (1991) 2924–2926.
 - [42] W. Bludau, A. Onton, W. Heinke, Temperature dependence of the band gap of silicon, *J. Appl. Phys.* 45 (1974) 1846–1848.
 - [43] J. Wang, Z. Gu, J. Zhang, X. Chen, M. Li, Y. Yu, M. Ge, X. Li, Mesoporous structure TiO₂/SiO₂ composite for methylene blue adsorption and photodegradation, *Micro Nano Lett.* 14 (2019) 323–328.
 - [44] D. Du, W. Shi, L. Wang, J. Zhang, Yolk-shell structured Fe₃O₄@void@TiO₂ as a photo-Fenton-like catalyst for the extremely efficient elimination of tetracycline, *Appl. Catal. B* 200 (2017) 484–492.
 - [45] H. Guo, N. Jiang, H. Wang, N. Lu, K. Shang, J. Li, Y. Wu, Degradation of antibiotic chloramphenicol in water by pulsed discharge plasma combined with TiO₂/WO₃ composites: mechanism and degradation pathway, *J. Hazard. Mater.* 371 (2019) 666–676.
 - [46] A. Vali, H.Z. Malayeri, M. Azizi, H. Choi, DPV-assisted understanding of TiO₂ photocatalytic decomposition of aspirin by identifying the role of produced reactive species, *Appl. Catal. B* 266 (2020), 118646.
 - [47] H. Wang, B. Liao, T. Lu, Y. Ai, G. Liu, Enhanced visible-light photocatalytic degradation of tetracycline by a novel hollow BiOCl@CeO₂ heterostructured microspheres: structural characterization and reaction mechanism, *J. Hazard. Mater.* 385 (2020), 121552.
 - [48] J. Yang, C.-Y. Mou, Ordered mesoporous Au/TiO₂ nanospheres for solvent-free visible-light-driven plasmonic oxidative coupling reactions of amines, *Appl. Catal. B* 231 (2018) 283–291.
 - [49] W. Shi, F. Guo, H. Wang, M. Han, H. Li, S. Yuan, H. Huang, Y. Liu, Z. Kang, Carbon dots decorated the exposing high-reactive (111) facets CoO octahedrons with enhanced photocatalytic activity and stability for tetracycline degradation under visible light irradiation, *Appl. Catal. B* 219 (2017) 36–44.
 - [50] C. Li, S. Yu, H. Dong, C. Liu, H. Wu, H. Che, G. Chen, Z-scheme mesoporous photocatalyst constructed by modification of Sn₃O₄ nanoclusters on g-C₃N₄ nanosheets with improved photocatalytic performance and mechanism insight, *Appl. Catal. B* 238 (2018) 284–293.